Nanoscale

COMMUNICATION

View Article Online
View Journal | View Issue

Check for updates

Cite this: *Nanoscale*, 2022, **14**, 10335

Received 2nd May 2022,
Accepted 26th June 2022

DOI: 10.1039/d2nr02395d

rsc.li/nanoscale

Understanding the role of surface interactions in the antibacterial activity of layered double hydroxide nanoparticles by atomic force microscopy†

Jazia Awassa, Samantha Soulé, Damien Cornu, Christian Ruby and Sofiane El-Kirat-Chatel *

Understanding the mechanisms of the interactions between zinc-based layered double hydroxides (LDHs) and bacterial surfaces is of great importance to improve the efficiency of these antibiotic-free antibacterial agents. In fact, the role of surface interactions in the antibacterial activity of zinc-based LDH nanoparticles compared to that of dissolution and generation of reactive oxygen species (ROS) is still not well documented. In this study, we show that ZnAl LDH nanoparticles exhibit a strong antibacterial effect against *Staphylococcus aureus* by inducing serious cell wall damages as revealed by the antibacterial activity tests and atomic force microscopy (AFM) imaging, respectively. The comparison of the antibacterial properties of ZnAl LDH nanoparticles and micron-sized ZnAl LDHs also demonstrated that the antibacterial activity of Zn-based LDHs goes beyond the simple dissolution into Zn^{2+} antibacterial ions. Furthermore, we developed an original approach to functionalize AFM tips with LDH films in order to probe their interactions with living *S. aureus* cells by means of AFM-based force spectroscopy (FS). The force spectroscopy analysis revealed that antibacterial ZnAl LDH nanoparticles show specific recognition of *S. aureus* cells with high adhesion frequency and remarkable force magnitudes. This finding provides a first insight into the antibacterial mechanism of Zn-based LDHs through direct surface interactions by which they are able to recognize and adhere to bacterial surfaces, thus damaging them and leading to subsequent growth inhibition.

Introduction

Despite the success achieved by the use of antibiotics to fight pathogenic bacteria, bacterial contamination and subsequent infections still present a significant threat to global health-care.[1] Moreover, the excessive use of traditional antibacterial drugs, *e.g.* antibiotics, has led to the emergence of antibiotic-resistant bacteria.[2,3] Recent developments in the field of materials science and nanotechnology have opened up new channels for the development of new inorganic antibiotic-free antibacterial agents as metallic nanoparticles (NPs),[4,5] silica NPs,[6,7] metal oxides NPs[8,9] and layered double hydroxides.[10,11]

Layered double hydroxides (LDHs) are clay lamellar solids consisting of stacks of positively charged brucite-like sheets comprising divalent and trivalent metal hydroxides. This net positive charge is actually compensated by the presence of negatively charged intercalating anions in the interlamellar region alongside water molecules.[12–15] Due to their interesting properties including their tunable composition, chemical stability, high anion exchangeability and biocompatibility, LDHs have been extensively studied as efficient antibacterial agents in different potential antibacterial applications such as water purification,[16] food packaging,[17,18] wound dressings,[19] and the textile industry.[20]

Recent studies have proved that pristine unmodified LDHs, in particular zinc-based LDHs, could induce an efficient antimicrobial effect without any further chemical modification.[16,21–25] We have recently reviewed the different antibacterial mechanisms of pristine LDHs.[26] The three main mechanisms proposed in the literature are: (1) membrane and cell wall damage by direct interactions with bacterial surfaces;[16,22,27,28] (2) release of constituent divalent metal ions;[16,21,22,24,27–29] and (3) generation of reactive oxygen species (ROS) which are well known to be toxic to the bacteria.[22,24,26,27,29] Despite the fact that these three hypotheses were proposed to explain the antimicrobial effect of pristine LDHs, the role of each antibacterial mechanism in the total antimicrobial action has not been determined because the proof of evidence from a real experimental setup is scarce. In our recent study,[21] we confirmed the contribution of the amount of the released zinc metal ions from Zn-based LDHs to their antibacterial activity (Mechanism 2). Zn-based LDHs

---

Université de Lorraine, CNRS, LCPME, F-54000 Nancy, France.
E-mail: elkirat1@univ-lorraine.fr

† Electronic supplementary information (ESI) available. See DOI: **https://doi.org/10.1039/d2nr02395d**

were able to release Zn^{2+} in broth media, and LDH samples having higher release profile of Zn^{2+} possessed the highest antibacterial activity. In fact, an increase in the Zn^{2+} ion concentration may disturb the permeability of bacterial membranes by changing their active normal transport system thus leading to their damage.[30] Although our previous finding supported the first suggested antibacterial mode of action of pristine LDHs by the release of divalent ions, this does not eliminate the possibility of the contribution of the other two suggested mechanisms, particularly, direct surface interactions with bacterial surfaces (Mechanism 1).

Bacterial adhesion to LDHs was previously investigated by standard adsorption isotherms, density-gradient separation techniques, and scanning and tunneling electron microscopy imaging.[19,31–34] Although these investigations admitted to the presence of direct surface interactions between LDHs and bacteria, almost none of them correlated such interactions to the antibacterial activity of LDHs as no antibacterial tests were carried out. In other words, adsorption or adhesion could not on its own explain the antibacterial activity. Moreover, only a few adhesion forces between bacteria and antibacterial clay materials or inorganic NPs were successfully measured by the atomic for microscopy (AFM) technique,[35,36] and as far as our knowledge goes none of them was performed to specifically decipher the antibacterial mechanisms of LDHs.

AFM is considered advantageous compared to other high-resolution techniques because it allows the analysis of samples in solutions, thus mimicking physiologically relevant conditions.[37] Thanks to the development of the AFM-based force spectroscopy (FS) approaches, the use of AFM is not only limited to being a powerful tool for high resolution imaging of bacterial cells but can also be used to probe bacterial adhesion phenomena.[38,39] In this context, AFM provides a quantitative evaluation of the adhesion interactions between bacteria and Zn-based antimicrobial LDHs which could yield a potential correlation with their antibacterial properties.

In order to measure LDH NP interactions with bacterial walls using AFM-based force spectroscopy (FS), two contact surfaces need to be created: a NP-functionalized AFM probe surface and a bacterial substrate surface to be probed. In fact, some studies reported the attachment of NPs on AFM probes using commercial glue adhesives.[40] However, if LDH NPs were to be attached to AFM probe using any type of glue, contamination may take place due to the possibility of glue adsorption on the surface thus leading to false adhesion force measurements. Another way to fix NPs on AFM tips is by chemical covalent functionalization using covalent linkers.[41–43] However, these chemical modifications may alter the LDHs' chemical nature and thus may in turn influence their interactions with bacteria. *In situ* deposition of NPs on the tips under an electron beam irradiation, evanescent wave illumination and short current-limited bias voltage have also been reported.[44–46] Nevertheless, the advanced devices required in such approaches may not be readily available, which hampers their generalization.

Therefore, a new suitable method to functionalize AFM tips with LDHs is necessary to probe the latter's interactions with bacteria and to understand their antibacterial mechanism. For this purpose, we designed an original approach to fabricate LDH-functionalized AFM tips by the *in situ* growth of LDH films directly on the surface of AFM tips. These LDH-functionalized tips were used to probe adhesion interactions with *Staphylococcus aureus* bacteria, a Gram-positive bacterium with multiple resistance strains that can infect humans leading to severe morbidity and mortality.[47,48]

The antimicrobial activity of ZnAl LDH NPs against *S. aureus* bacteria was determined by the agar disk diffusion and broth microdilution methods and compared with the effect of MgAl LDH NPs and micron-sized ZnAl LDHs. The comparison between the antibacterial properties of nano-sized and micron-sized ZnAl LDHs showed that the antibacterial properties of the ZnAl LDH NPs go beyond the simple dissolution of Zn^{2+} ions and is also related to surface contact interactions. Furthermore, AFM imaging revealed that growth inhibition by ZnAl LDH NPs was associated with severe morphological cell wall damages whereas cells treated with MgAl LDH NPs remained intact. Then, we took advantage of our original approach to grow LDH films *in situ* on AFM tips and to probe the interaction between LDHs and living *S. aureus* cells using the AFM-based FS approach. The physico-chemical characterization based on X-ray diffraction (XRD) and Fourier-transform infra-red (FT-IR) spectroscopy revealed that LDH films presented properties comparable to those of LDH NPs. As compared to the controls, the FS adhesion maps recorded with ZnAl LDH-functionalized tips presented strong adhesion (hundreds of pN) at a high frequency which suggested that the antimicrobial effect of Zn-based LDH NPs is at least partly due to specific and direct interactions with the bacterial cell wall. This study provides valuable insights into the correlation between the specific ability of Zn-based LDHs to adhere to bacterial surfaces and their capability to inhibit the growth of bacteria.

Results and discussion

Structural and textural properties of ZnAl and MgAl LDH NPs

Nitrate-intercalated ZnAl and MgAl LDH NPs were prepared by the coprecipitation-hydrothermal method described elsewhere.[49] The $M^{II} : Al^{III}$ molar ratios of ZnAl and MgAl LDH NPs evaluated by the inductively coupled plasma mass spectroscopy (ICP-MS) analysis were found to be 1.94 and 1.97, respectively. The obtained values were very close to the expected value of 2, thus corresponding potentially to the ideal arrangement of M^{II} and Al^{III} cations in brucite-like sheets.[21]

Fig. 1a shows the XRD patterns of the prepared MgAl and ZnAl LDH NPs, both having the characteristic reflections of LDH materials exhibiting a hexagonal lattice with a rhombohedral 3R symmetry and no further crystalline impurities.[50] The interlayer spacing of both LDH NPs extracted from the diffraction peaks at the (003) and (006) basal reflections was 0.89 ±

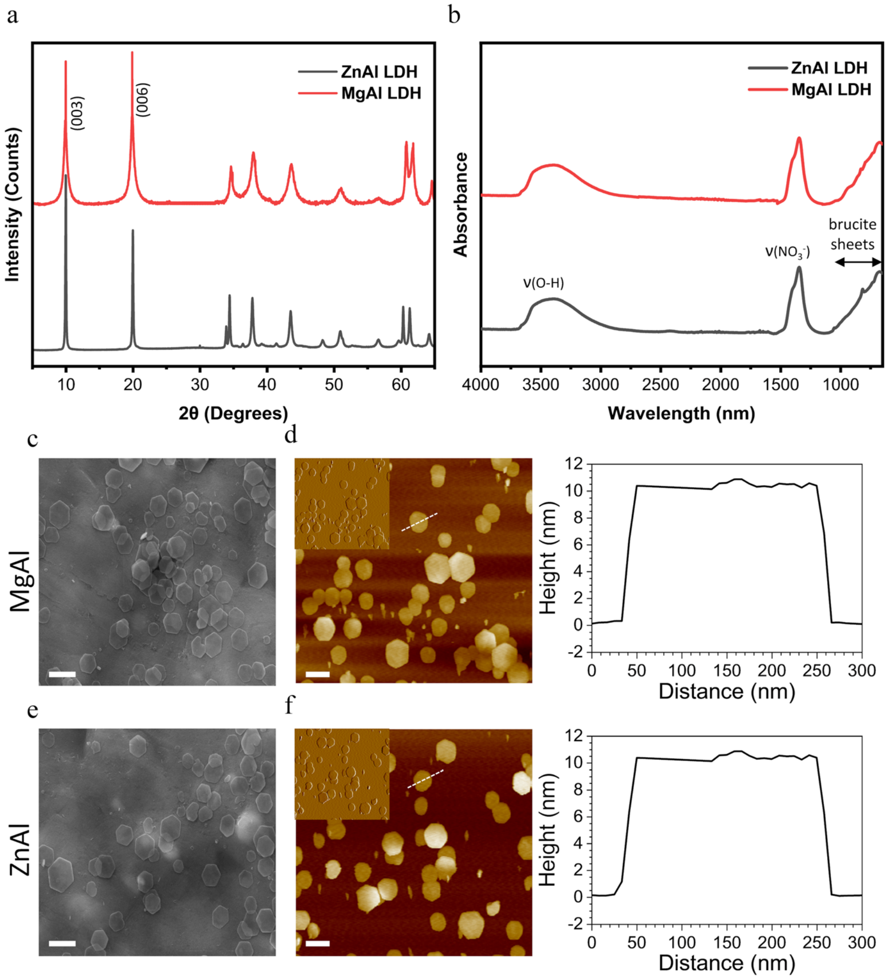

Fig. 1 NPs characterization. (a) XRD patterns of MgAl and ZnAl NPs. (b) FT-IR spectra of MgAl and ZnAl NPs. (c and e) SEM images of MgAl (c) and ZnAl (e) NPs (scale bar = 200 nm). (d and f) AFM height images of MgAl (d) and ZnAl (f) NPs (scale bar = 200 nm, insets are deflection images showing the NPs surface ultra-structure) together with height profiles of single particles. Dashed lines marked on the height images represent the sections used to determine the height profiles.

0.01 nm, which is in good agreement with the interlayer spacing values for nitrate-intercalated LDHs.[51,52] Similarly, the FT-IR spectra of both LDH NPs showed the characteristic peaks of nitrate-intercalated LDHs corresponding to the O–H stretching vibrations at 3446 cm^{-1} and NO_3^- vibration at 1350 cm^{-1} (Fig. 1b).[53] No additional vibration bands which could be assigned to the amorphous impurity phases had been detected, suggesting the high purity of our prepared NPs.

X-ray photoelectron spectroscopy (XPS) was further carried out to confirm the chemical composition and bonding states of MgAl and ZnAl LDH NPs (Fig. S1 and S2†). N 1s, Al 2p, and O 1s peaks located respectively at about 406.5, 74.5 and 532 eV were found in both MgAl and ZnAl LDH NPs (Fig. S1a and S2a†). The presence of the N 1s peak is ascribed to the NO_3^- intercalating anions.[54] The Al 2p region (Fig. S1b and S2b†) illustrates the presence of Al(III) species in both samples.[55] The O 1s signal peak can be separated into three peaks located at about 530 eV, 532 eV and 533 eV (Fig. S1c and S2c†), which are attributed to the lattice oxygen, hydroxyl groups and water molecules, respectively.[55–57] Moreover, the XPS spectra of MgAl NPs show the presence of the Mg 2p peak at ~50.5 eV (Fig. S1d†) accounting for the constituent Mg(II) divalent metal.[58] On the other hand, the presence of Zn(II) constituent divalent metals in ZnAl NPs was confirmed by the presence of Zn $2p_{1/2}$ and Zn $2p_{3/2}$ located at ~1044 and ~1021 eV respectively.[54] Therefore, such configurations account for the typical MgAl and ZnAl LDH structures as suggested by XRD and FT-IR analyses.

Both MgAl and ZnAl NPs presented a hexagonal lamellar structure as revealed by their SEM and AFM images (Fig. 1). Both LDH NPs possessed similar average particle sizes (obtained as an average of the particle sizes of 100 LDH NPs) extracted from their SEM images (172 ± 31 nm and 176 ± 44 nm, for MgAl and ZnAl NPs, respectively). Similar average particle size values (obtained as an average of the particle sizes of 100 LDH NPs) of 169 ± 35 nm for MgAl NPs and 171 ± 38 nm for ZnAl NPs were obtained from their AFM height images. The height profiles revealed that our synthesized NPs also had a similar average whole thickness (obtained as an average of the thicknesses of 100 LDH NPs) of 10.6 ± 0.4 and 10.4 ± 0.7 nm, for MgAl and ZnAl LDH NPs, respectively. Such a thickness unambiguously implied the multilamellar nature (~12 layers) of the synthesized NPs.[59]

ZnAl LDH NPs exert an efficient antibacterial effect against *S. aureus*

The antibacterial activity of ZnAl and MgAl LDH NPs against *S. aureus* was first evaluated by agar disk diffusion method. The generated inhibition zone diameters and their mean values obtained from three repetitive trials are presented in Fig. 2a and b. Broth microdilution turbidimetric tests were also carried out to determine the minimum inhibitory concentration (MIC) required to inhibit the growth of *S. aureus* by ZnAl and MgAl LDHs (Fig. 2c).

ZnAl LDH NPs showed an efficient antibacterial effect against *S. aureus* with an average inhibition zone diameter of 20.6 mm and MIC value of 93.8 μg mL^{-1}. On the other hand, MgAl LDH NPs did not provide any antibacterial activity revealed by any of the two antibacterial tests, and thus played the role of a negative control in this case. The superior antibacterial activity of ZnAl LDH NPs could be attributed to the nature of their constituent divalent metal, *e.g.* Zn^{2+}.[21] In fact, it was previously reported that zinc-based NPs have a strong antibacterial effect towards a broad range of bacteria.[25] Such an effect may be achieved by adhering to bacteria, changing its charge distribution and blocking the transport of nutrients into and out of the membrane, or else by binding to bacterial intracellular DNA leading to its denaturation.[25,60]

The antibacterial activity of the prepared ZnAl LDH NPs against *S. aureus* was slightly higher than that reported by Dutta *et al.* for ~250 nm-sized ZnAl LDHs having a MIC value of 200 μg mL^{-1} against *S. aureus*,[22] yet remarkably superior to that of micron-sized Zn-based LDHs prepared by Lobo-Sánchez *et al.*(MIC value of 10 000 μg mL^{-1}).[24] On the other hand, Zn-based LDH NPs having a particle size ~50 nm reported by Moaty *et al.* presented a MIC value of 15.6 μg mL^{-1} against the same bacterial strain, which is superior to that of our ZnAl LDH NPs.[16] Such a difference in the antibacterial activity should be interpreted very cautiously, since many parameters play a role in the antibacterial properties of LDHs including the different physicochemical properties of different strains and differences in the experimental procedures used to demonstrate the antibacterial test assays.

In our previous experiments performed with identical antibacterial test procedures,[21] we showed that the antibacterial activity of micron-sized ZnAl LDHs (particle size ~1 μm) was related to the released Zn^{2+} ions (Mechanism 2) which was found to be 3.3% relative to the total amount of metal zinc ions initially present in the nitrate-intercalated ZnAl LDHs. Consequently, the tested LDH sample showed an inhibition zone diameter of 11 mm. On the other hand, the partial dissolution profile of Zn^{2+} released out of ZnAl LDH NPs (particle size ~167 nm) used in this study was found to be 6%. Interestingly, the increase in the inhibition zone diameters for ZnAl LDH NPs used in this study was almost of the same order (2 times) as that of the increased amount of released zinc ions. The fact that these augmentations fall in the same range indicates that the enhanced antibacterial performance of ZnAl NPs in the agar disk diffusion test can be related to Zn^{2+} release in broth media. By design, inhibition zones are related to the diffusion of the released cations,[26] which is in agreement with our finding.

In contrast, the MIC value can be impacted by all the antimicrobial mechanisms, *i.e.* surface interactions and ROS generation.[26] In this case, the MIC of ZnAl LDH NPs (93.8 μg mL^{-1}) used in this study was almost 16 times greater than that obtained previously for micron-sized ZnAl LDH (MIC = 1500 μg mL^{-1}).[21] Taking into consideration that similar antibacterial tests assay protocols against the same strain were adopted in both studies, the increase in Zn^{2+} release by a factor of 2 cannot by itself explain the enhanced antibacterial activity of ZnAl LDH NPs. In fact, this seems to be more related to the lateral crystal size of LDHs which was reduced by almost 6

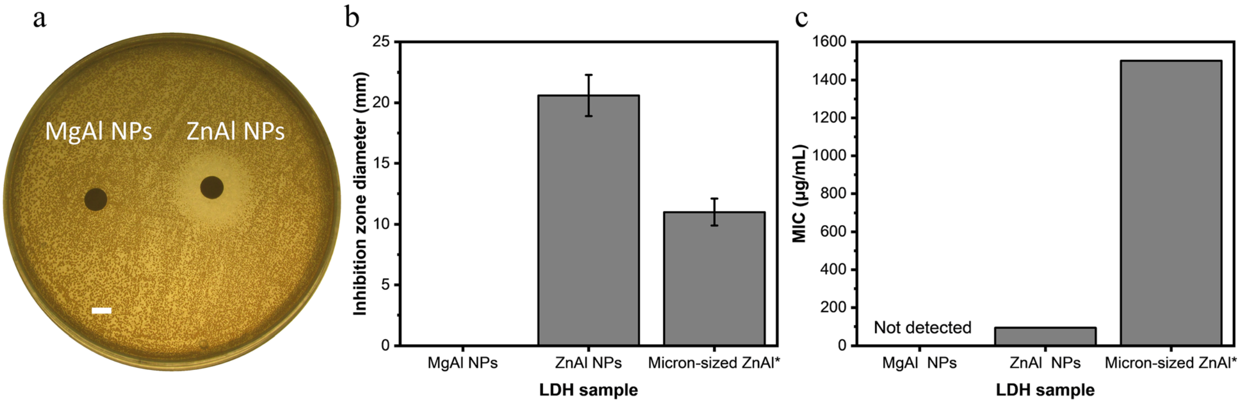

Fig. 2 NPs antibacterial activity against *S. aureus*. (a) Agar disk diffusion test using 10 mg mL^{-1} ZnAl and MgAl NPs suspensions (scale bar = 5 mm). (b) Mean zone of inhibition of MgAl, ZnAl NPs and micron-sized ZnAl LDH calculated as the average inhibition diameters of three repetitive trials. (c) MIC values for MgAl, ZnAl NPs and micron-sized ZnAl LDH calculated as the average MIC of three repetitive trials. *Data for micron-sized ZnAl LDH are adapted from our previous study.[21]

times in the case of ZnAl NPs compared to that in micron-sized LDHs used previously. Additionally, the great difference in MIC values between micron-sized particles and our newly synthesized NPs could also be related to the ability of NPs to provide a stable mobile suspension in solution, whereas micron-sized LDH particles were sedimented. This provides the evidence concerning the role of surface interactions in the antibacterial effect of LDHs (Mechanism 1). In this context, smaller size LDHs were able to induce an enhanced antibacterial effect due to their larger surface area (in this case, the surface area is 36 times greater for the NPs) and greater mobility of the NPs in a stable suspension promoting more accessible surface and contact with the tested *S. aureus* bacteria.[26,29,61]

Finally, it is important to mention that the contribution of ROS generation to the antibacterial activity of our ZnAl LDH NPs (Mechanism 3) could be eliminated since all experiments were performed inside an incubator in the absence of light and the production of ROS by LDHs is only pronounced in the presence of a suitable light source.[26]

ZnAl LDH NPs affect the morphology of *S. aureus* cells

AFM imaging was used to visualize the surface topography of *S. aureus* cells before and after the treatment with ZnAl and MgAl LDH NPs at a concentration of 93.8 μg mL^{-1}, which corresponds to the MIC value of ZnAl LDH NPs. Additionally, the roughness parameter R_q (root mean square of the heights) was obtained from the AFM images of the top of the bacteria at a high magnification of 400 × 400 nm^2 scanning areas. The measured roughness parameter for all treated/untreated cells was obtained for a similar area to that of the high magnification AFM images, *e.g.* 400 × 400 nm^2 (512 samples/line; 262 144 data points).

As shown in Fig. 3a and b, untreated cells as well as those treated with non-antibacterial MgAl LDH NPs presented regular spheroid morphologies and smooth surfaces (R_q = 15.9 ± 0.6 nm, 16.8 ± 0.8 nm, for untreated and MgAl NPs-treated cells, respectively). The obtained R_q values seemed to be greater than those previously obtained in the literature,[62,63] probably due to the different bacterial immobilization method, selected area of measurement and/or the AFM imaging conditions.

On the other hand, cells treated with antibacterial ZnAl LDH NPs were completely distorted with highly corrugated surfaces presenting hollows and crests (Fig. 3c). Similar cell damage observations were previously reported.[63–65] Moreover, cells treated with ZnAl LDH NPs were found to have 3 times rougher surfaces (R_q = 49.5 ± 0.7 nm) than the untreated and

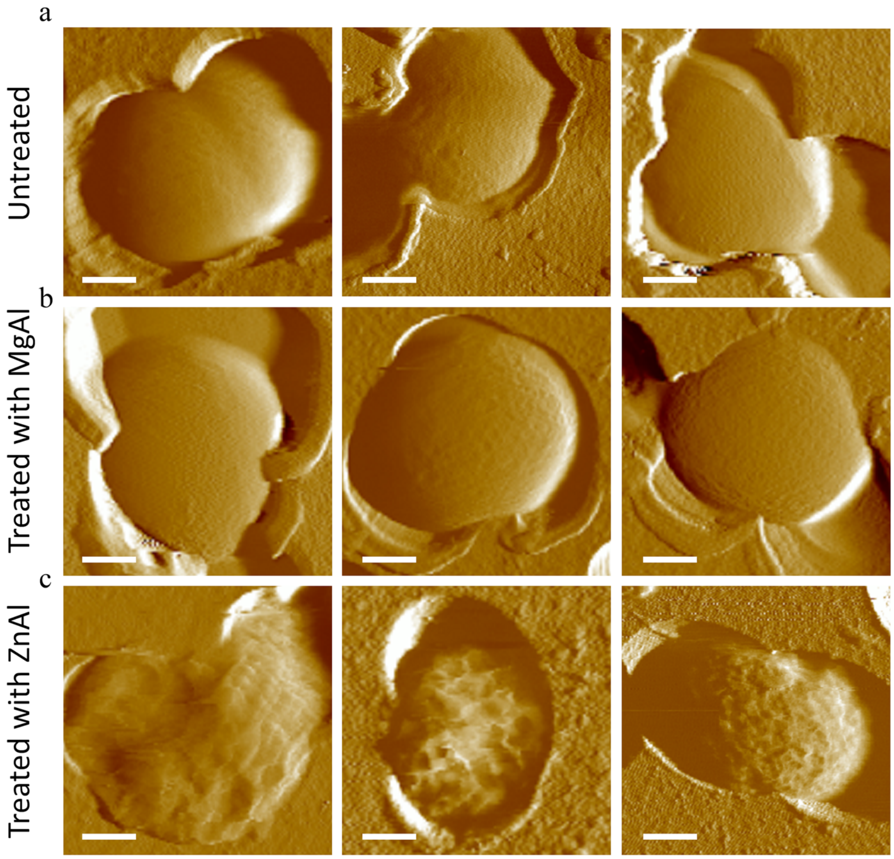

Fig. 3 AFM deflection images of *S. aureus* in liquid (scale bar = 250 nm). (a) Untreated *S. aureus* cells. (b) *S. aureus* cells treated with MgAl LDH NPs at MIC value of ZnAl LDH NPs. (c) *S. aureus* cells treated with ZnAl LDH NPs at MIC.

MgAl LDH NP treated cells. The increase in surface roughness of bacteria suggests the existence of cell wall damage induced by ZnAl LDH NPs,[62,63] which could be eventually followed by cell lysis and subsequent leakage of intracellular components.[65]

To examine the morphological impacts of antibacterial ZnAl LDH on a greater fraction of cells, *S. aureus* were immobilized on mica substrates and imaged in air (Fig. S3†). Although imaging in air is not physiologically relevant, it can enhance morphological features and help to differentiate topographical differences between cells.[66] Untreated and MgAl NPs treated *S. aureus* cells appeared on the mica surface as grape-like clusters of round cocci with homogeneous cellular shapes and regular surfaces. The diameter of cells observed in clusters varied from 600 to 1080 nm and the average value was 752 ± 115 nm, typical of this type of microorganism.[67,68] Upon treating *S. aureus* with antibacterial ZnAl LDH NPs, nearly all cells presented abnormal shapes and irregular surfaces. Some cells were enlarged in diameter (~1400 nm) suggesting that the cellular swelling due to the ZnAl NP treatment. Other cells appeared completely distorted with deep grooves, crests, hollows and even some split surfaces. Finally, some cells were completely disrupted or lysed leaving behind some cell debris covering the mica substrate.

The corresponding height profiles of bacterial cells immobilized on the mica substrate were also determined (Fig. S4†). Cells treated with MgAl NPs showed a height profile of 480 ± 45 nm quite similar to that of healthy untreated cells (445 ± 19 nm). In contrast, *S. aureus* cells treated with ZnAl LDH NPs presented a lower height profile (180 ± 77 nm), suggesting their collapse. Consequently, cells treated with antibacterial ZnAl LDH NPs did not only exhibit a different morphology than that of healthy untreated ones but also different height profiles as well. A similar effect was previously noted for damaged *Escherichia coli* cells.[65]

All these observations suggest that ZnAl LDH NPs induce an antibacterial effect on *S. aureus* cells by targeting their cell wall leading to its damage, swelling or collapse, leakage of intracellular components and subsequently to the death of the microorganism.[63–65]

AFM tips can be functionalized with LDH films

Surface interactions occurring at the interface between bacteria and ZnAl LDH NPs are probably a main contributor to the antibacterial effect. In order to decipher the role of surface interactions in the antibacterial activity of ZnAl LDH NPs by AFM-based FS, AFM tips were functionalized with LDHs. This was performed by growing LDH films directly on the surface of silicon nitride AFM tips. However, since it is quite difficult to perform LDH characterization directly on AFM tips, the characterization was done on LDH films initially grown on silicon wafers. ZnAl and MgAl LDH films were synthesized on aluminum coated silicon wafers by the *in situ* growth method described elsewhere.[69] The obtained $M^{II}:Al^{III}$ molar ratios evaluated by the ICP-MS analysis for ZnAl and MgAl LDH films were 2.1 and 2.05, respectively. These values correspond again very well to the expected $M^{II}:Al^{III}$ molar ratio of 2, similar to that for nano-sized and micron-sized[21] ZnAl and MgAl LDHs.

The XRD patterns of the synthesized ZnAl and MgAl LDH films exhibited the characteristic (003) and (006) basal reflections of the LDH structure, which confirmed the formation of the LDH film on the silicon wafer (Fig. S5a†). The interlayer spacing of both LDH films was 0.89 ± 0.01 nm, which is in perfect agreement with the interlayer spacing values for nitrate-intercalated LDHs and their previously synthesized NP counterparts.[51,52] The quasi-absence of non-basal reflections at high angles implied the *c*-oriented growth of LDH crystallites in the film.[70,71] Similarly, the FT-IR spectra of ZnAl and MgAl films also confirmed the successful growth of nitrate-intercalated LDH films without any amorphous impurity phases (Fig. S3b†).

The morphology of the LDH films and LDH-functionalized AFM tips were examined by SEM imaging. As shown in Fig. 4a and b, MgAl and ZnAl LDHs were successfully grown on the surface of silicon wafers with their *c*-axis mostly perpendicular to the substrate. The morphology of the observed structures showed a "cauliflower-like" shape, very similar to that reported by other groups,[72,73] using a comparable *in situ* growth wet-chemistry synthesis method. Electron dispersive X-ray spectroscopy (EDS) was further performed on the LDH films (Fig. S6†) which ensured the growth of LDH films on silicon wafers with a $M^{II}:Al^{III}$ molar ratio similar to that determined by ICP analysis (Table S1†).

The thickness of the formed films was determined by cross-sectional SEM imaging and was found to be 312 ± 24 nm and 315 ± 25 nm for MgAl film and ZnAl LDH films, respectively (Fig. S3c and e†). Scratch method was also used to determine the thickness of the obtained films by AFM imaging and the obtained values (314 ± 10 nm and 316 ± 12 nm for MgAl film and ZnAl LDH films, respectively) were in good agreement with those found by SEM imaging (Fig. S3d and f†).

Similar synthesis conditions were adapted to grow LDH films on silicon nitride AFM tips, where a bare silicon nitride tip was first coated with aluminum (Fig. 4c and d). ZnAl and MgAl LDH films were then grown directly on the surface of the aluminum-coated tips (Fig. 4e and f). The morphology of the LDH films grown on the tips was similar to that of those grown on silicon wafers. However, the hexagonal particles in this case seemed to be less defined probably due to the pyramidal geometry of the tip. The successful functionalization of AFM tips with MgAl and ZnAl LDH films with a $M^{II}:Al^{III}$ molar ratio ~2 similar to that obtained on LDH films grown on silicon wafers was also confirmed by EDS analysis (Fig. S7 and Table S1†).

Force spectroscopy reveals specific surface interactions between antibacterial zinc-based LDHs and *S. aureus*

Single living *S. aureus* cells were probed by ZnAl-functionalized tips using AFM-based FS. Fig. 5a–c and 6b shows adhesion maps and adhesion force and rupture length histograms as well as representative force–distance (FD) curves obtained between different *S. aureus* cells and ZnAl tips. Adhesive pixels

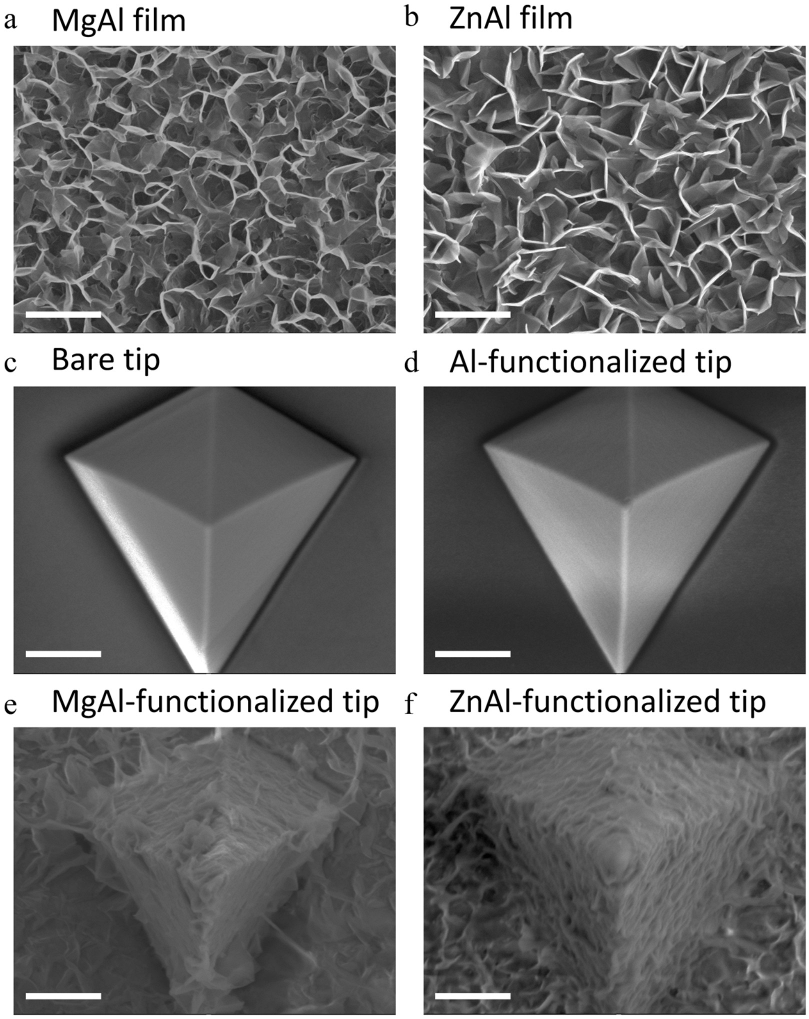

Fig. 4 SEM images of LDH films on silicon wafers and AFM tips (scale bar = 1 μm). (a) MgAl LDH film grown on silicon wafer. (b) ZnAl LDH film grown on silicon wafer. (c) Bare silicon nitride AFM tip. (d) Al-Functionalized silicon nitride AFM tip. (e) MgAl LDH-functionalized silicon nitride AFM tip. (f) ZnAl LDH-functionalized silicon nitride AFM tip.

were randomly distributed on the maps suggesting the homogeneous adhesion of ZnAl LDH to the host cell surface. Most recorded FD curves showed an adhesion signature with a frequency ranging from 63 to 93% (Fig. 5b and 6b). The variation in adhesion frequencies among the probed cells may be attributed to the slight heterogeneity in cell wall microarchitecture and composition or else to the position of the ZnAl-functionalized AFM tips during measurements. Measured adhesion forces of all cells mainly ranged from 180 to 800 pN (Fig. 5b and 6b) with rupture lengths ranging between 10 and 300 nm (Fig. 5c). Such a finding indicates that ZnAl tips were able to recognize *S. aureus* cell wall with high adhesion frequency, thus suggesting the presence of surface interactions occurring at the interface between ZnAl LDHs and the bacterial cell wall.

To determine whether the presented surface interactions between ZnAl LDHs and *S. aureus* are specifically related to their antibacterial properties, the adhesion behavior of ZnAl-functionalized tips was compared to that of control Al-coated tips as well as to that of non-antibacterial MgAl-functionalized ones. For this purpose, individual living *S. aureus* cells trapped in porous membranes (Fig. 6a) were probed using the three different AFM tips, *e.g.* ZnAl-functionalized, MgAl-functionalized and Al-functionalized tips.

Upon probing the same cells (Fig. 6a) using Al-functionalized tips, no considerable adhesion between aluminum and *S. aureus* was noticed, wherein the adhesion frequencies and force magnitudes did not exceed 11% and 280 pN (Fig. 6b), respectively. This indicates that the constituent aluminum trivalent metal ions do not contribute to the observed adhesion surface interactions between ZnAl LDH and the cell wall of *S. aureus*.

MgAl-functionalized tips adopting quite similar morphologies to those of ZnAl-functionalized ones (Fig. 4e and f) were also used to probe the cell surfaces of *S. aureus*. This was actually done for two main reasons. First, to eliminate the

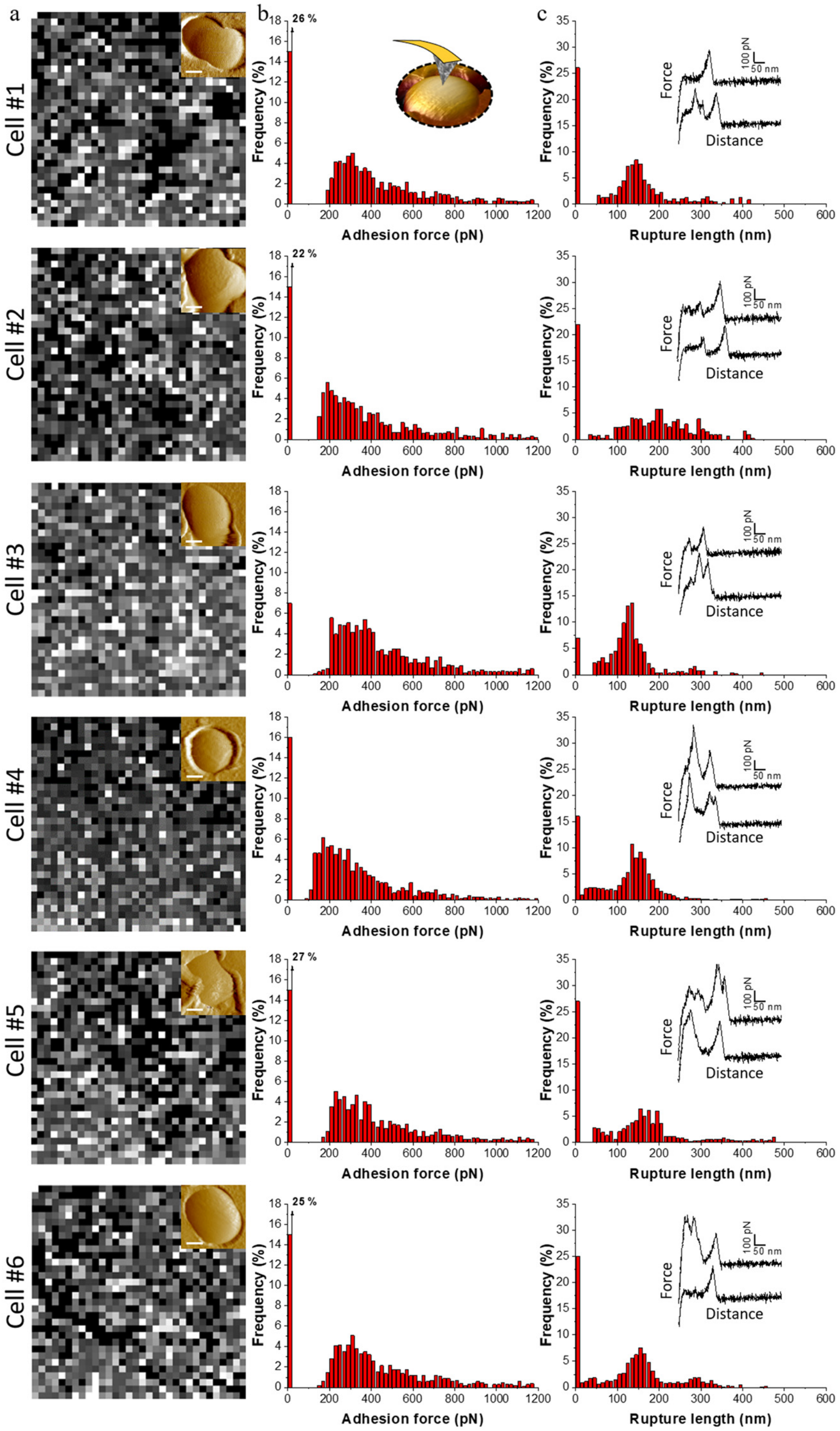

Fig. 5 Force spectroscopy on live *S. aureus* cells with ZnAl-functionalized AFM tips. (a) Adhesion maps (400 × 400 nm^2) recorded on *S. aureus* cells (insets are AFM deflection images of probed cells, scale bar = 250 nm) with ZnAl-functionalized AFM tips. White/grey pixel correspond to adhesive events and black pixels correspond to non-adhesive events (scale 0–1000 pN). (b and c) Corresponding adhesion force (b) and rupture length (c) histograms together with representative force–distance curves. Data were obtained from four independent experiments using different tips and independent cell cultures.

possibility of the contribution of the LDH-functionalized tip's morphology to the reliability of our force measurements. Second, to determine whether the observed surface interactions between the cell wall of *S. aureus* and ZnAl LDHs are specific to Zn-based LDHs and to further link them to their demonstrated antibacterial properties.

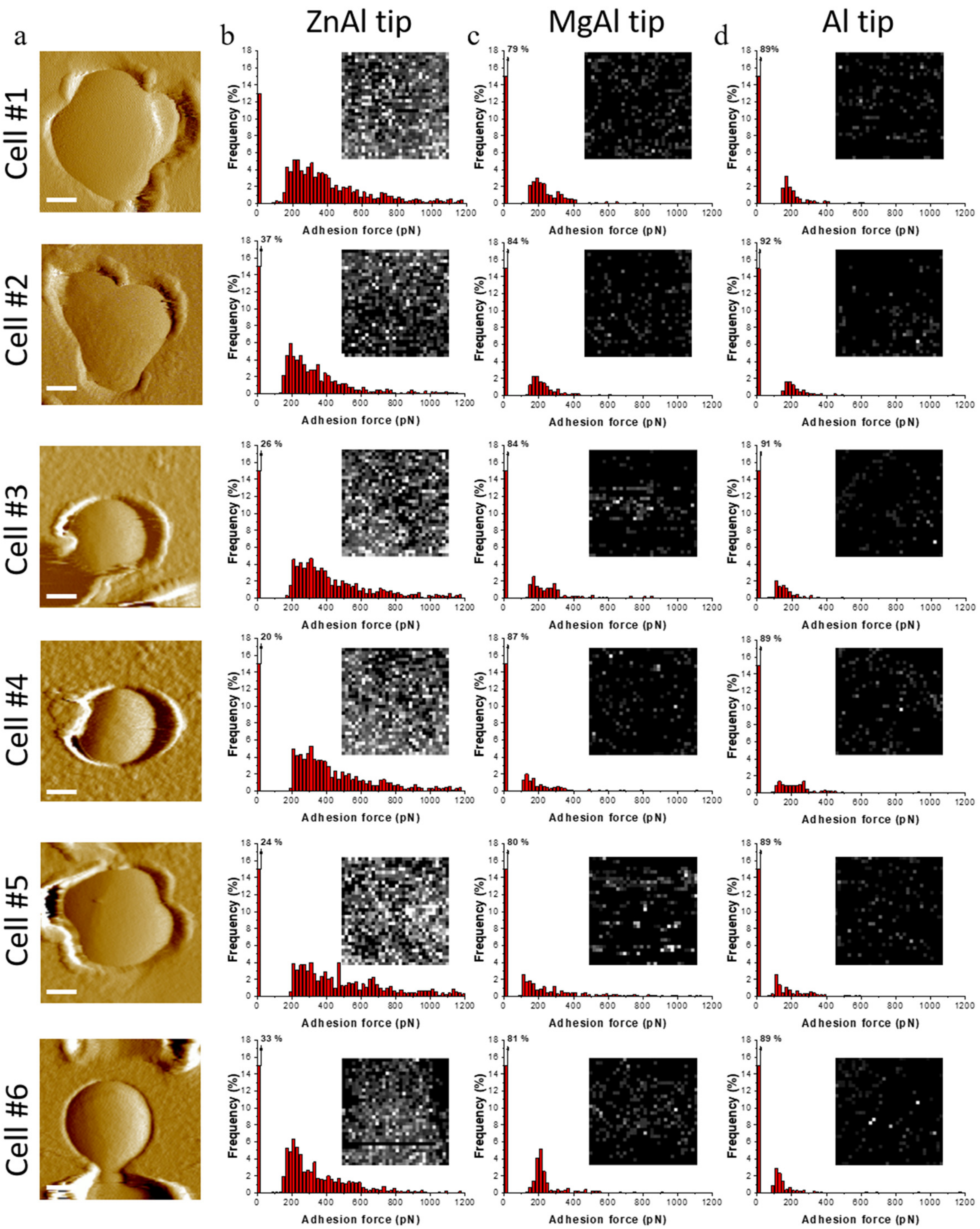

Fig. 6 Force spectroscopy with functionalized tips reveals specific interaction for ZnAl tips. (a) Topography images of *S. aureus* cells trapped in porous membranes (scale bar = 250 nm) and probed with functionalized AFM tips. (b–d) Adhesion force histograms and adhesion force maps (insets, 400 × 400 nm^2) obtained on the top of cells using ZnAl-functionalized AFM tip (b) MgAl-functionalized AFM tip (c) Al-functionalized AFM tip (d). White/grey pixel correspond to adhesive events and black pixels correspond to non-adhesive events (scale 0–1000 pN). Data were obtained from four independent experiments using different tips and independent cell cultures.

Although cells probed with MgAl-functionalized tips showed slightly higher adhesion frequencies (13–21%) and force magnitudes (150–300 pN) in comparison with Al-functionalized tips, their adhesion behavior in terms of both adhesion frequencies and force magnitudes were remarkably weaker than those of ZnAl-functionalized tips. This indicates that our LDH functionalization protocol did not impose critical complications to the consistency of our force measurements even when the morphology of the AFM tip was modified.

At the end of each experiment, both LDH-functionalized tips were washed with ethanol, dried with nitrogen and imaged again by SEM. The functionalized tips seemed to be intact after being in contact with the bacteria during the experiments (Fig. S8†) thus confirming the robust functionalization protocol used.

We had previously established in this work that ZnAl LDH NPs possessed specific and superior antibacterial properties in comparison with non-antibacterial MgAl LDH NPs, which was validated by *S. aureus* growth inhibition (Fig. 2) and imposing serious morphological impact on their cell walls (Fig. 3 and Fig. S1†). Therefore, the specific adhesion interactions observed for antibacterial ZnAl LDHs provided a first insight about the contribution of direct contact interactions to the antibacterial activity of Zn-based LDHs (Mechanism 1). In fact, the sensitivity of microorganisms to different divalent metal-based materials is actually dependent on several factors, including the role each metal plays in normal metabolism, and the presence of specific binding sites for each metal.[74,75] *S. aureus* cells were highly sensitive to ZnAl LDHs probably due to the antibacterial role played by their constituent zinc components, where they showed strong surface adhesion interactions with the tested bacterial membranes. In this context, ZnAl LDH NPs were specifically able to recognize and adhere to *S. aureus* cells thus imposing serious damages to their cell walls by direct surface interactions.

Conclusion

In the present study, the role of surface interactions (Mechanism 1) in the antibacterial activity of ZnAl LDH NPs was studied. ZnAl LDH NPs exhibited specific antibacterial activity against *S. aureus* in comparison with non-antibacterial MgAl LDH. The evidence of the contribution of surface interactions to the antibacterial activity of LDHs was provided by the superior antibacterial activity of nano-sized ZnAl LDH NPs compared to that of micron-sized ZnAl LDHs. For similar quantities, agar disk diffusion showed an inhibition zone two times larger and broth microdilution antibacterial assays showed that the MIC was 16 times lower for ZnAl NPs, showing an effect beyond the simple dissolution into Zn^{2+} antibacterial ions. Therefore, direct contact interactions have to be considered, which is evidenced by serious morphological impacts including membrane distortion, swelling and dissociation into cell debris which were observed on the surface of *S. aureus* cells upon being treated with ZnAl LDH NPs at MIC.

In addition, LDH-functionalized AFM tips were prepared and used to probe surface adhesion interactions between the cell surface and LDHs by AFM-based FS. ZnAl-functionalized AFM tips were able to recognize the cell wall of *S. aureus* cells with high adhesion frequencies. Additionally, the comparison of the adhesion behavior of three different AFM tips, *e.g.* Al-coated, MgAl functionalized and ZnAl-functionalized, indicated the presence of specific surface interactions between ZnAl LDHs and *S. aureus* cells. Such a finding suggested the presence of a strong correlation between the specific ability of zinc-based LDHs to adhere and damage bacterial cell walls, thus supporting the previously suggested antibacterial mechanism of pristine LDHs by direct surface interactions (Mechanism 1).

Experimental part

LDH NPs synthesis

Nitrate-intercalated ZnAl and MgAl LDHs were synthesized by the coprecipitation-hydrothermal method, adapted from Xu *et al.*[49] Briefly, a mixture of 2 mmol $M(NO_3)_2 \cdot 6H_2O$ (M = Zn, Mg; Sigma-Aldrich) and 1 mmol $Al(NO_3)_3 \cdot 9H_2O$ (Sigma-Aldrich) with a total volume of 10 mL was very quickly added to 40 mL of 0.15 M NaOH solution (VWR Chemicals), under a nitrogen atmosphere and vigorous stirring for 10–30 minutes. The LDH slurry was obtained by centrifugation at 10 000 rpm, washed twice and dispersed again in 50 mL of decarbonated water. The resultant suspension was then transferred to a stainless-steel autoclave with a Teflon lining and heated at 80 °C for 24 h. LDH NP powder was then obtained by centrifugation and air drying at 80 °C.

Synthesis of LDH films and LDH-functionalized AFM tips

Nitrate-intercalated ZnAl and MgAl LDH films were synthesized on aluminum coated silicon wafers by the *in situ* growth method adapted from Zhang *et al.*,[69] with some slight modifications. Silicon wafers were first cleaned with piranha solution, washed thoroughly with water and ethanol, and then coated by plasma sputtering (Q15OT S, Quorum) with a thin layer of aluminum (~10 nm). $M(NO_3)_2 \cdot 6H_2O$ (M = Zn, Mg; 2.5 mmol) and NH_4NO_3 (30 mmol, Sigma-Aldrich) were dissolved in deionized water (50 mL), and 1% ammonia solution was then slowly added until the pH reached 6.5 and 9.5 for ZnAl and MgAl LDH films respectively. This solution was transferred to a stainless-steel autoclave with a Teflon lining in which the coated aluminum samples were immersed. The autoclave was heated for 24 h at 80 °C. The obtained LDH films grown on silicon wafers were then washed with distilled water and ethanol, then dried in air at room temperature. A similar procedure was followed to synthesize LDH-functionalized AFM silicon nitride probes in which LDHs were *in situ* grown on MLCT-C (Bruker Corporation) AFM tips.

$M^{II}:Al^{III}$ molar ratio determination

$M^{II}:Al^{III}$ molar ratios of LDH NPs and films were measured by inductively coupled plasma mass spectroscopy (ICP-MS Agilent-7800). LDH NPs and films were dissolved in 1% HNO_3. The detected isotopes were ^{27}Al, ^{66}Zn, and ^{26}Mg.

X-ray diffraction measurements

X-ray diffraction (XRD) characterization was performed using a Panalytical X'Pert Pro MPD diffractometer in the reflection geometry using Cu radiation (Kα_1 = 1.5406 Å), a Ge(111) incident-beam monochromator, Soller slits of 0.02 rad, programmable divergence and anti-scatter slits. The irradiated area was fixed to 10 × 10 mm^2, and an X'Celerator detector was used. All diffraction data were collected using the same procedure, *i.e.* at the same scattering angle range (between 5 and 60°) with a 0.0167° step and a speed of 1° min^{-1}. The interlamellar distance of both LDH NPs and films was extracted from the (003) and (006) basal reflections which is equal to d(003) and d(006)/2.

Infrared spectroscopy measurements

Infrared spectra of LDH NPs were recorded in the mid-infrared range on a Bruker Vertex 70v spectrometer equipped with a KBr beam-splitter and a deuterated triglycine sulfate (DTGS) detector. An attenuated total reflection (ATR) accessory (Platinum ATR with a single reflection diamond crystal, Bruker) was used and the spectral resolution was 4 cm^{-1} and the accumulation time was 1 min (100 scans). Compartments containing the detector and the ATR accessory were under vacuum (<1 hPa). Infrared spectra of LDH films were recorded under nitrogen flow in a transmission mode on a FT-IR Nicolet 8700 spectrometer equipped with a KBr beam splitter and a DTGS thermal detector. The reference was an aluminum coated Si wafer for LDH films. LDH film spectra were recorded and processed using the OMNIC 8.1.0.10 software (Thermo Fisher Scientific Inc.).

X-ray photoelectron spectroscopy

A photoelectron spectrometer (Kratos Axis Ultra DLD, Manchester, Royaume-Uni) equipped with a degassing chamber under ultra-vacuum, a storage room and an analysis chamber UHV under ultra-vacuum was used to obtain the XPS spectra of LDH NPs. Samples were deposited on a conductive copper belt, inserted on the transfer bar, introduced into a degassing chamber and then to the analysis chamber which was equipped with a monochromatic X-ray source Al Kα emission at 1486.6 eV. Electron counting and detection were performed by a delay line detector DLD (Delay-Line Detector, 115 channels). Spectra were recorded at a normal angle (90°) between the surface of the sample and the direction of ejected electrons. The acquisition of low-resolution spectra has been carried out with pass energy of 160 eV at steps of 1 eV and the high-resolution spectra with pass energy of 20 eV at steps of 0.5 eV. The analyzed area for all samples was fixed at 0.3 × 0.7 mm^2. Samples were corrected for charging effects using the C 1s peak. The spectra were adjusted by the Shirley baseline by two models of peak compounds: 70% of Gaussian function and 30% of Lorentzian function.

Scanning electron microscopy imaging

The morphology of LDH NPs, films and LDH-functionalized AFM tips was examined by scanning electron microscopy (SEM) performed on a JEOL JSM-IT500HR combined to an electron-dispersive X-ray spectrometer (EDS), with a Field Emission Gun (FEG) and a voltage of analysis situated in between 2 kV and 10 kV. The analysis was performed under high vacuum, and 60 μm diaphragm aperture was settled. Secondary Electron Detector (SED) was used for imaging. In order to determine the thickness of the formed LDH films, similar SEM imaging conditions were applied to image lateral cross-sections of LDH films. The average particle size of MgAl and ZnAl LDH nanoparticles was obtained from their respective SEM images, calculated as an average particle size of 100 LDH NPs. The elemental composition and M^{II} : Al^{III} molar ratio of MgAl and ZnAl LDH films and functionalized films was determined by EDS analysis.

Antibacterial activity tests

The antibacterial activity of the ZnAl and MgAl LDH NPs was evaluated using agar disc diffusion and broth microdilution turbidity methods against Gram-positive *S. aureus* strain 187 (HER 1239) provided by Félix d'Hérelle Reference Center for Bacterial Viruses from the Université Laval (Québec, Canada).

Inhibition zone diameters generated by MgAl and ZnAl LDH powders were determined by agar disk diffusion test. *S. aureus* cells were precultured in 5 mL sterile TSB (SIGMA ALDRICH) overnight at 37 °C and then diluted to 1/1500 in sterile Phosphate Buffered Saline (PBS, SIGMA ALDRICH). Then, 250 μL of diluted bacterial suspension was spread on sterilized TSB agar Petri dishes using sterile cotton tipped swabs (COPAN) to prepare a homogeneous bacterial layer. Antibiotic filter disks of (diameter = 6 mm, Dominique Dutscher) were placed on the dishes and 20 μL of LDH dispersions (10 mg mL^{-1}) were loaded on the respective disks. Petri dishes were then incubated at 37 °C for 24 h. Afterwards, bacterial inhibition zones were observed around the disks. The diameter of the circular zones was measured using a centimeter ruler and mean values of three repeated trials were recorded and represented in millimeters.

Broth microdilution turbidimetric method was used to determine the minimum inhibitory concentration (MIC) of the prepared ZnAl and MgAl LDH powders. *S. aureus* cells were precultured in 5 mL TSB overnight at 37 °C. An inoculum of *S. aureus* was then prepared and diluted to obtain an optical density of 0.1 at λ = 600 nm (OD$_{600}$ = 0.1). ZnAl and MgAl LDH powders were dispersed in TSB and two-fold dilution series were then prepared in a 96-well micro-titer plate. Each well included 25 μL of the diluted LDH powder and 175 μL of bacterial inoculum. Un-inoculated broth wells containing the different used LDH dispersion concentrations were used as a negative standard growth control. As a positive control, 12 wells were prepared with 175 μL of bacterial inoculum and 25 μL of TSB. The micro-titer plate was then sealed with parafilm and incubated at 37 °C under agitation for 48 hours. The MIC value for both LDH samples was recognized as the lowest concentration that had no visible turbidity.

Partial dissolution of ZnAl NPs into Zn^{2+}

Partial dissolution profile of the ZnAl LDH NPs into their Zn^{2+} was evaluated by dispersing 10 mg mL^{-1} of the NPs in Tryptic Soy Broth (TSB). After a given incubation time of 24 hours at

37 °C, the supernatants were collected by centrifugation. Finally, the metal concentration in the supernatant was measured by ICP-MS (Agilent-7800).

Atomic force microscopy (AFM) imaging and force spectroscopy

All AFM experiments were performed at room temperature using Bioscope Resolve AFM (Bruker corporation, Santa Barbara, CA) and the spring constants of the used cantilevers were determined using the thermal noise method.[76]

LDH NPs immobilized on silicon substrates and LDH films were imaged in peak-force tapping mode using SNL-C tips (Bruker corporation) in air. LDH NPs were dispersed in an ethanol solution, sonicated for 30 min and deposited on clean silicon substrates and dried at 30 °C overnight. The average particle size and thickness of MgAl and ZnAl LDH nanoparticles was obtained from their respective AFM height images, calculated as an average particle size of 100 LDH NPs.

For topography images on *S. aureus*, cells were cultivated alone (untreated) or with (treated) MIC of ZnAl and MgAl LDH NPs during 24 h in TSB at 37 °C. For imaging in MOPS ((3-(*N*-morpholino)propane sulfonic acid, Sigma) buffer solution, stationary phase cultures of *S. aureus* were centrifuged, washed twice in MOPS and filtered into porous polycarbonate membranes (pore size = 0.8 μm, Millipore). After filtration and rough rinsing, a 1 × 1 cm^2 piece of membrane was cut and attached with double sided adhesive tape at the bottom of a Petri dish and immersed in MOPS. The roughness parameter R_q (root mean square of the heights) of the cells was calculated using the commercial Nanoscope analysis (Bruker) from AFM images performed on the top of bacteria at a high magnification of 400 × 400 nm^2 scanning areas. The measured roughness parameter for all treated/untreated cells was performed on a similar area to that of the high magnification AFM images, *e.g.* 400 × 400 nm^2 (512 samples/line; 262 144 data points).

For imaging in air, cells were centrifuged, washed twice and resuspended in ultra-pure distilled water then deposited on mica substrates. After 2 hours, substrates were gently rinsed in ultrapure distilled water and dried overnight at 30 °C. For both air and liquid conditions, images were acquired in peak-force tapping mode using SNL-C tips.

For force measurements on cells using AFM-based force spectroscopy, stationary phase cultures of *S. aureus* were trapped in porous membranes in a similar procedure used for cells imaging in MOPS. First, bare MLCT-C tips were used to localize and image individual cells. Then, the tips were replaced by aluminum-coated tips, MgAl and ZnAl LDH-functionalized tips. Adhesion force maps and histograms were obtained by recording 32 × 32 force–distance curves on areas of 400 × 400 nm^2 on cells surfaces, calculating the adhesion force of the last adhesion peak for each force curve, and displaying the value as a grey pixel. All curves were recorded using a maximum applied force of 250 pN, a contact time of 250 ms, and constant approach and retraction speeds of 1 μm s^{-1}. Data were processed using the commercial Nanoscope analysis (Bruker) and MATLAB (The MathWorks, Natick, MA) software.

At the end of each experiment, both LDH-functionalized tips were washed with ethanol, dried with nitrogen and imaged again using SEM.

Conflicts of interest

There are no conflicts of interest to declare.

Acknowledgements

We would like to acknowledge the spectroscopy and microscopy Service Facility of SMI LCPME (Université de Lorraine-CNRS– **https://www.lcpme.cnrs-nancy.fr**). Claire Genois from LCPME (Université de Lorraine-CNRS– **https://www.lcpme.cnrs-nancy.fr**) is particularly acknowledged for the ICP-MS analysis. We would also like to thank the plateforme PMD^{2}X de l'Institut Jean Barriol de l'Université de Lorraine, in particular Pierrick Durand for the XRD analysis. Jazia Awassa acknowledges the French Ministry of Higher Education for her PhD grant.

Financial support was received from the French Ministry of Higher Education (MESR), and the French National Scientific Centre (CNRS).

References

1 S. Dhingra, N. A. A. Rahman, E. Peile, M. Rahman, M. Sartelli, M. A. Hassali, T. Islam, S. Islam and M. Haque, *Front. Public Health*, 2020, **8**, 535668.
2 E. Christaki, M. Marcou and A. Tofarides, *J. Mol. Evol.*, 2020, **88**, 26.
3 C. Nathan, *Nat. Rev. Microbiol.*, 2020, **18**, 259–260.
4 M. Sousa de Almeida, E. Susnik, B. Drasler, P. Taladriz-Blanco, A. Petri-Fink and B. Rothen-Rutishauser, *Chem. Soc. Rev.*, 2021, **50**, 5397.
5 M. Guerrero Correa, F. B. Martínez, C. P. Vidal, C. Streitt, J. Escrig and C. L. de Dicastillo, *Beilstein J. Nanotechnol.*, 2020, **11**, 1450.
6 V. Selvarajan, S. Obuobi and P. L. R. Ee, *Front. Chem.*, 2020, **8**, 602.
7 H. Song, Y. Ahmad Nor, M. Yu, Y. Yang, J. Zhang, H. Zhang, C. Xu, N. Mitter and C. Yu, *J. Am. Chem. Soc.*, 2016, **138**, 6455.
8 L. Shkodenko, I. Kassirov and E. Koshel, *Microorganisms*, 2020, **8**, 1545.
9 M. Li, Z. P. Xu, Y. Sultanbawa, W. Chen, J. Liu and G. Qian, *Colloids Surf., B*, 2019, **181**, 585.
10 C. Forano, F. Bruna, C. Mousty and V. Prevot, *Chem. Rec.*, 2018, **18**, 1150.
11 G. Mishra, B. Dash and S. Pandey, *Appl. Clay Sci.*, 2018, **153**, 172.

12 L. Mohapatra and K. Parida, *J. Mater. Chem. A*, 2016, **4**, 10744.

13 P. Nalawade, B. Aware, V. J. Kadam and R. S. Hirlekar, *J. Sci. Ind. Res.*, 2009, **68**, 267.

14 V. Rives, *Layered double hydroxides: present and future*, Nova Science Publishers, Huntington, N.Y, 2001.

15 F. L. Theiss, G. A. Ayoko and R. L. Frost, *Appl. Surf. Sci.*, 2016, **383**, 200.

16 S. A. A. Moaty, A. A. Farghali and R. Khaled, *Mater. Sci. Eng., C*, 2016, **68**, 184.

17 H. Cheng, X. Gao, K. Zhang, X. Wang, W. Zhou, S. Li, X. Cao and D. Yan, *New J. Chem.*, 2019, **43**, 19408.

18 L. Tammaro, V. Vittoria and V. Bugatti, *Eur. Polym. J.*, 2014, **52**, 172.

19 W. Zhang, Y. Zhao, W. Wang, J. Peng, Y. Li, Y. Shangguan, G. Ouyang, M. Xu, S. Wang, J. Wei, H. Wei, W. Li and Z. Yang, *Adv. Healthcare Mater.*, 2020, **9**, 2000092.

20 S. Mallakpour, Z. Radfar and C. M. Hussain, *Appl. Clay Sci.*, 2021, **206**, 106054.

21 J. Awassa, D. Cornu, S. Soulé, C. Carteret, C. Ruby and S. El-Kirat-Chatel, *Appl. Clay Sci.*, 2022, **216**, 106369.

22 S. Dutta, T. K. Jana, S. K. Halder, R. Maiti, A. Dutta, A. Kumar and K. Chatterjee, *ChemistrySelect*, 2020, **5**, 6162.

23 A. M. León-Vallejo, F. D. Velázquez-Herrera, Á. Sampieri, G. Landeta-Cortés and G. Fetter, *Appl. Clay Sci.*, 2019, **180**, 105194.

24 M. Lobo-Sánchez, G. Nájera-Meléndez, G. Luna, V. Segura-Pérez, J. A. Rivera and G. Fetter, *Appl. Clay Sci.*, 2018, **153**, 61.

25 F. Peng, D. Wang, D. Zhang, H. Cao and X. Liu, *Appl. Clay Sci.*, 2018, **165**, 179.

26 J. Awassa, D. Cornu, C. Ruby and S. El-Kirat-Chatel, *Colloids Surf., B*, 2022, **217**, 112623.

27 M. Li, L. Li and S. Lin, *Chin. Chem. Lett.*, 2020, **31**, 1511.

28 H. A. Tabti, M. Adjdir, A. Ammam, B. Mdjahed, B. Guezzen, A. Ramdani, C. K. Benddedouche, N. Bouchikhi and N. Chami, *Res. Chem. Intermed.*, 2020, **46**, 5377.

29 G. Mishra, B. Dash, S. Pandey and D. Sethi, *Appl. Clay Sci.*, 2018, **165**, 214.

30 W. Fan, Q. Sun, Y. Li, F. R. Tay and B. Fan, *J. Nanobiotechnol.*, 2018, **16**, 10.

31 S. Jin, P. H. Fallgren, J. M. Morris and Q. Chen, *Sci. Technol. Adv. Mater.*, 2007, **8**, 67.

32 J. Liu, C. Duan, J. Zhou, X. Li, G. Qian and Z. P. Xu, *Appl. Clay Sci.*, 2013, **75–76**, 39.

33 T. Alekseeva, V. Prevot, M. Sancelme, C. Forano and P. Besse-Hoggan, *J. Hazard. Mater.*, 2011, **191**, 126.

34 D. Wang, F. Peng, J. Li, Y. Qiao, Q. Li and X. Liu, *Mater. Today*, 2017, **20**, 238.

35 W. Zhang, A. G. Stack and Y. Chen, *Colloids Surf., B*, 2011, **82**, 316.

36 Q. Huang, H. Wu, P. Cai, J. B. Fein and W. Chen, *Sci. Rep.*, 2015, **5**, 16857.

37 A. Beaussart, C. Feuillie and S. El-Kirat-Chatel, *Nanoscale*, 2020, **12**, 23885.

38 A. Beaussart and S. El-Kirat-Chatel, *Cell Surf.*, 2019, **5**, 100031.

39 S. A. James, N. Hilal and C. J. Wright, *Biotechnol. J.*, 2017, **12**, 1600698.

40 Q. K. Ong and I. Sokolov, *J. Colloid Interface Sci.*, 2007, **310**, 385–390.

41 X. Liu, *Langmuir*, 2018, **34**, 10774.

42 I. U. Vakarelski, S. C. Brown, B. M. Moudgil and K. Higashitani, *Adv. Powder Technol.*, 2007, **18**, 605.

43 I. U. Vakarelski and K. Higashitani, *Langmuir*, 2006, **22**, 2931.

44 O. Sqalli, I. Utke, P. Hoffmann and F. Marquis-Weible, *J. Appl. Phys.*, 2002, **92**, 1078.

45 T. Okamoto and I. Yamaguchi, *J. Microsc.*, 2001, **202**, 100.

46 H. Cheng, Y. Chang, S. Tang, C. Yuan, J. Tang and F. Tseng, *Nanoscale Res. Lett.*, 2013, **8**, 482.

47 F. D. Lowy, *J. Clin. Invest.*, 2003, **111**, 1265.

48 S. J. van Hal, S. O. Jensen, V. L. Vaska, B. A. Espedido, D. L. Paterson and I. B. Gosbell, *Clin. Microbiol. Rev.*, 2012, **25**, 362.

49 Z. P. Xu, G. Stevenson, C. Lu and G. Max Lu, *J. Phys. Chem. B*, 2006, **110**, 16923.

50 F. Cavani, F. Trifirò and A. Vaccari, *Catal. Today*, 1991, **11**, 173.

51 S. Marappa, S. Radha and P. V. Kamath, *Eur. J. Inorg. Chem.*, 2013, **2013**, 2122.

52 F. Z. Mahjoubi, A. Khalidi, M. Abdennouri and N. Barka, *J. Taibah Univ. Sci.*, 2017, **11**, 90.

53 R. Zhu, X. Zhu, Y. Zhu, Z. Wang, X. He, Z. Wu, L. Xue, W. Fan, R. Huang, Z. Xu, X. Qi, W. Xu, Y. Yu, Y. Ren, C. Li, Q. Cheng, L. Ling, S. Wang and L. Cheng, *ACS Nano*, 2021, **15**, 2812.

54 W. Bao, H. Tian, Y. Jiang, K. Zhu, R. Zhang, Y. Tan, W. Li, Z. Yu and L. Wang, *Ionics*, 2019, **25**, 3859.

55 Z. Zhang, Z. Hua, J. Lang, Y. Song, Q. Zhang, Q. Han, H. Fan, M. Gao, X. Li and J. Yang, *CrystEngComm*, 2019, **21**, 4607.

56 B. Xiao, W. Zhu, Z. Li, J. Zhu, X. Zhu and G. Pezzotti, *R. Soc. Open Sci.*, 2018, **5**, 180867.

57 P. Li, Y. Jiao, S. Yao, L. Wang and G. Chen, *New J. Chem.*, 2019, **43**, 3139.

58 S. Kundu and M. K. Naskar, *Mater. Adv.*, 2021, **2**, 3600.

59 Z. Liu, R. Ma, M. Osada, N. Iyi, Y. Ebina, K. Takada and T. Sasaki, *J. Am. Chem. Soc.*, 2006, **128**, 4872.

60 G. Vimbela, S. M. Ngo, C. Fraze, L. Yang and D. A. Stout, *Int. J. Nanosci.*, 2017, **12**, 3941.

61 G. Mishra, B. Dash, S. Pandey and P. P. Mohanty, *J. Environ. Chem. Eng.*, 2013, **1**, 1124.

62 J. Wu, Z. Chu, Z. Ruan, X. Wang, T. Dai and X. Hu, *Front. Physiol.*, 2018, **9**, 1658.

63 H. Li, Q. Chen, J. Zhao and K. Urmila, *Sci. Rep.*, 2015, **5**, 11033.

64 K. Sahu, H. Bansal, C. Mukherjee, M. Sharma and P. K. Gupta, *J. Photochem. Photobiol., B*, 2009, **96**, 9.

65 M. Mathelié-Guinlet, C. Grauby-Heywang, A. Martin, H. Février, F. Moroté, A. Vilquin, L. Béven, M.-H. Delville

and T. Cohen-Bouhacina, *J. Colloid Interface Sci.*, 2018, **529**, 53.

66 F. Quilès, I. Accoceberry, C. Couzigou, G. Francius, T. Noël and S. El-Kirat-Chatel, *Nanoscale*, 2017, **9**, 13731.

67 E. B. Tatlybaeva, H. N. Nikiyan, A. S. Vasilchenko and D. G. Deryabin, *Beilstein J. Nanotechnol.*, 2013, **4**, 743.

68 A. Beaussart, C. Retourney, F. Quilès, R. Dos Santos Morais, C. Gaiani, H.-P. Fiérobe and S. El-Kirat-Chatel, *J. Colloid Interface Sci.*, 2021, **582**, 764.

69 F. Zhang, L. Zhao, H. Chen, S. Xu, D. G. Evans and X. Duan, *Angew. Chem., Int. Ed.*, 2008, **47**, 2466.

70 L. Wang, C. Li, M. Liu, D. G. Evans and X. Duan, *Chem. Commun.*, 2007, 123.

71 X. Guo, F. Zhang, S. Xu, D. G. Evans and X. Duan, *Chem. Commun.*, 2009, 6836.

72 D. Scarpellini, C. Falconi, P. Gaudio, A. Mattoccia, P. G. Medaglia, A. Orsini, R. Pizzoferrato and M. Richetta, *Microelectron. Eng.*, 2014, **126**, 129.

73 J. Liu, X. Huang, Y. Li, K. M. Sulieman, X. He and F. Sun, *J. Phys. Chem. B*, 2006, **110**, 21865.

74 G. Borkow and J. Gabbay, *Comput. Mater. Contin.*, 2005, **12**, 2163.

75 M. R. Bruins, S. Kapil and F. W. Oehme, *Ecotoxicol. Environ. Saf.*, 2000, **45**, 198.

76 J. L. Hutter and J. Bechhoefer, *Rev. Sci. Instrum.*, 1993, **64**, 1868.